

Lagrangian study of the final warming in the southern stratosphere during 2002: Part I. The Vortex Splitting at Upper Levels

J. Curbelo C. R. Mechoso A. M. Mancho S. Wiggins

Abstract

The present two-part paper provides a Lagrangian perspective of the final southern warming in 2002, during which the stratospheric polar vortex (SPV) experienced a unique splitting. Part I focuses on the understanding of fundamental processes for filamentation and ultimately for vortex splitting on a selected isentropic surface in the middle stratosphere. Part II discusses the three-dimensional evolution of the selected sudden warming event. We approach the subject from a dynamical systems viewpoint and search for Lagrangian coherent structures using a Lagrangian descriptor as a tool. In this Part I we work in the idealized framework of a kinematic model that allows for an understanding of the contributing elements of the flow in late September during the splitting. We introduce a definition of kinematic SPV boundary based on a criterion for binning parcels inside and outside the vortex according to their values of the Lagrangian descriptor and associated PDF. This definition is justified by using arguments that go beyond heuristic considerations based on the potential vorticity. Next, we turn to the filamentation processes along this kinematic boundary, and the role of Lagrangian structures in the SPV splitting. We determine a criterion for splitting based on the structure of the evolving unstable and stable manifolds.

Keywords: Stratospheric sudden warming, vortex boundary, Kinematic models, filamentation, vortex split

1 Introduction

We study the behaviour of the stratospheric polar vortex (SPV) in the southern hemisphere during the final warming in spring (September-November) of 2002. This particular warming followed an evolution that was quite different from the norm as described by [1] and reviewed by [2]. The SPV experienced a unique splitting at upper levels in late September, after which it reformed with a weaker strength to finally transition into the summer circulation. Several papers present detailed *Eulerian* diagnoses of this final warming and vortex splitting [3, 4, 5, 6, 2, 7, 8, 9, 10, 11]. The present two-part paper gives a *Lagrangian* perspective of the event.

In this Part I we concentrate on a single potential temperature level in the middle stratosphere. The analysis is carried out in the idealized framework of a two-dimensional (2D) kinematic model (KM). The KM aims at emulating the behavior of the longest planetary waves on an isentropic surface as obtained from the reanalysis data, and allows for a detailed parametric study that is greatly facilitated by the dynamical systems approach. According to our previous work [12], a 2D KM with an appropriate choice of functional and geometrical features and model parameters can capture the fundamental mechanisms responsible for the complex fluid parcel evolution during polar vortex filamentation and breakdown. The work in the KM framework has two main objectives. The first is to explore a kinematic definition for the SPV boundary that can be justified, at least partially, with arguments that go beyond heuristic considerations based on the potential vorticity (PV) field as is generally done. Such a definition will be used in Part II for the selection of parcel trajectories that can help visualize the 3D evolution of the event. The second objective is to determine a criterion for vortex splitting based on the evolving Lagrangian structures. Such a criterion will help in Part II to understand why the vortex splitting only occurred at some levels.

We start in section 2 with snapshots of *Eulerian* features of the flow during the selected final warming event using a reanalysis dataset. Section 3 outlines our methodology presenting the Lagrangian descriptor and describing the KM. Section 4 introduces a definition for the vortex boundary based on the Lagrangian descriptor. Section 5 discusses a criterion for SPV split based on the evolving Lagrangian structures. Finally, section 6 presents a summary and the conclusions. Annex A is a succinct review of Lagrangian concepts used in the paper.

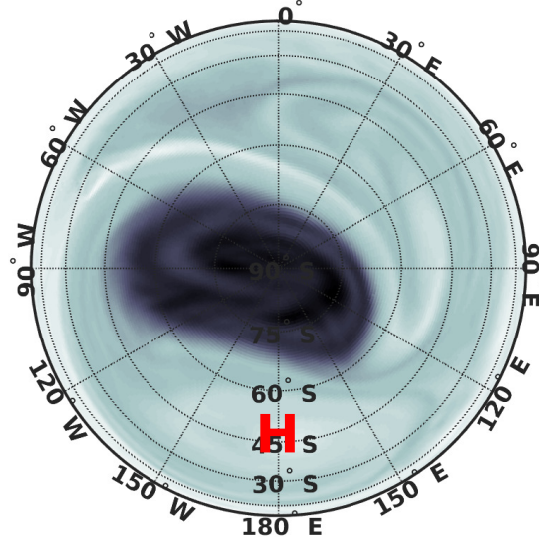
2 The southern final warming in Spring 2002

In this section we compile a selection of outstanding *Eulerian* features of the flow observed during the southern stratospheric final warming event of 2002. All figures in the present paper that refer to observed features are obtained using the ERA-Interim reanalysis dataset produced by the European Centre for Medium-Range Weather Forecasts (ECMWF; [13]). Figure 1 displays PV maps at 850K in the middle stratosphere at distinct stages of the final warming. PV is given by,

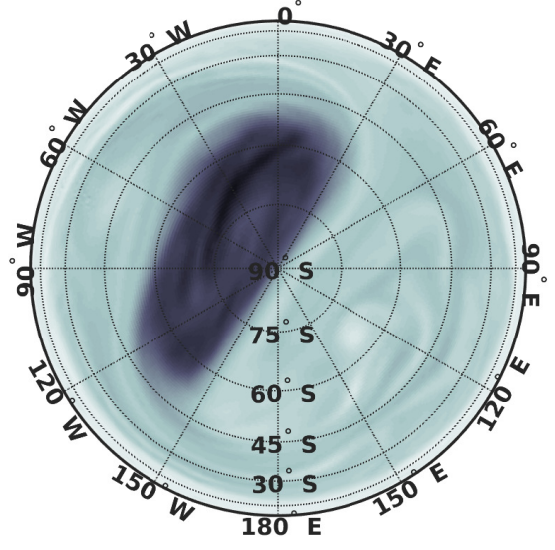
$$PV = -g(f + \zeta_\theta) \frac{\partial \theta}{\partial p} \quad (1)$$

where f is the Coriolis parameter, ζ_θ is relative vorticity on the isentropic surface θ , and $\frac{\partial \theta}{\partial p}$ is a measure of static stability. This expression includes only the vertical component of the vorticity and uses the hydrostatic assumption. At the 850K level, the SPV in the early part of the period (September 9) was in a circumpolar configuration, albeit its center was slightly displaced from the South Pole, while an anticyclone had developed over the

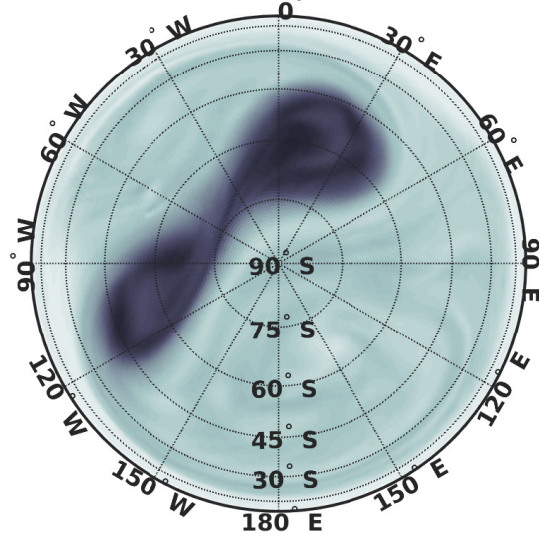
(a) 9 September 2002



(b) 22 September 2002



(c) 24 September 2002



(d) 15 October 2002

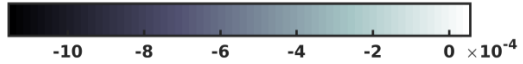
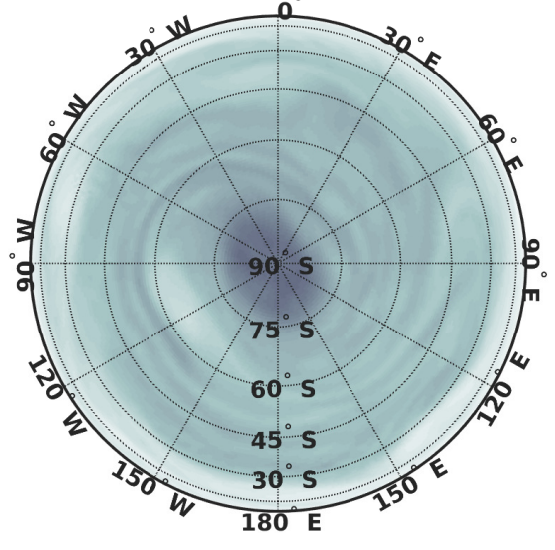


Figure 1: Maps of potential vorticity at 850K for distinct stages of the southern final warming in 2002. Units are $\text{K m}^2\text{kg}^{-1}\text{s}^{-1}$. The red letter 'H' in (a) indicates the anticyclonic center over the Southern Pacific

southern Pacific Ocean. A dramatic series of events ensued, during which the cyclonic vortex strongly elongated and split into two (September 22 and 24, respectively). The two cyclonic vortices resulting from the splitting evolved further in time while interacting with each other, until one of them set in a polar position and the other disappeared as a separate entity. By 15 October a weak cyclonic circulation remained around the pole without a robust structure at 850K.

A complementary view of the event is provided in Figure 2 for the 10 hPa level ($\sim 850\text{K}$). The upper part of panel (a) in this figure represents the zonal velocity averaged along latitudinal lines (zonal-mean zonal wind), showing strong westerlies at high southern latitudes until 2 days before an abrupt change in direction to easterlies around September 22. The lower part of panel (a) displays the sharp increase of zonal mean temperatures in the polar region associated to this event. These changes in velocities and temperature represent the only documented sudden stratospheric warming in the Southern Hemisphere on record. Panel (b) shows that planetary waves in the southern stratosphere were very active during the southern spring of 2002, particularly in September. Within the ten-day period centered on September 22, the upper part of panel (b) shows that the amplitude of wave 1 almost doubled, while the amplitude of wave 2 decreased, albeit not so drastically. The lower part of panel (b) confirms that wave 1 was quasi-stationary and wave 2 propagated eastward, as is typical in the southern stratosphere during early spring [14, 15, 16]. The period of wave 2 is around 19 days which gives a zonal angular phase speed of approximately $9.5^\circ/\text{day}$. We note that increased amplitude of wave 1 results in a displacement of the SPV from a circumpolar configuration, while increased amplitude of wave 2 results in a stretching of the SPV in one direction and contraction (or “pinching”) in the orthogonal direction.

3 Methodology

3.1 The Lagrangian descriptor function M

As in our previous studies on the southern SPV ([17, 12], [18]) we follow an approach based on dynamical systems theory by searching for dynamical objects from which the general behaviour of particles can be deduced. Among these objects are hyperbolic trajectories and their invariant manifolds as well as others defined in the Annex.

Our principal analysis tool for stratospheric studies is the Lagrangian descriptor known as the function M . In the following paragraph we define this tool and give our motivation for its selection. The function M is given by the expression,

$$M(\mathbf{x}_0, t_0, \tau) = \int_{t_0-\tau}^{t_0+\tau} \|\mathbf{v}(\mathbf{x}(t; \mathbf{x}_0), t)\| dt, \quad (2)$$

where $\mathbf{v}(\mathbf{x}, t)$ is the velocity field and $\|\cdot\|$ denotes the Euclidean norm. At a given time t_0 , M corresponds to the length of the trajectory of a fluid parcel that starts at x_0 and

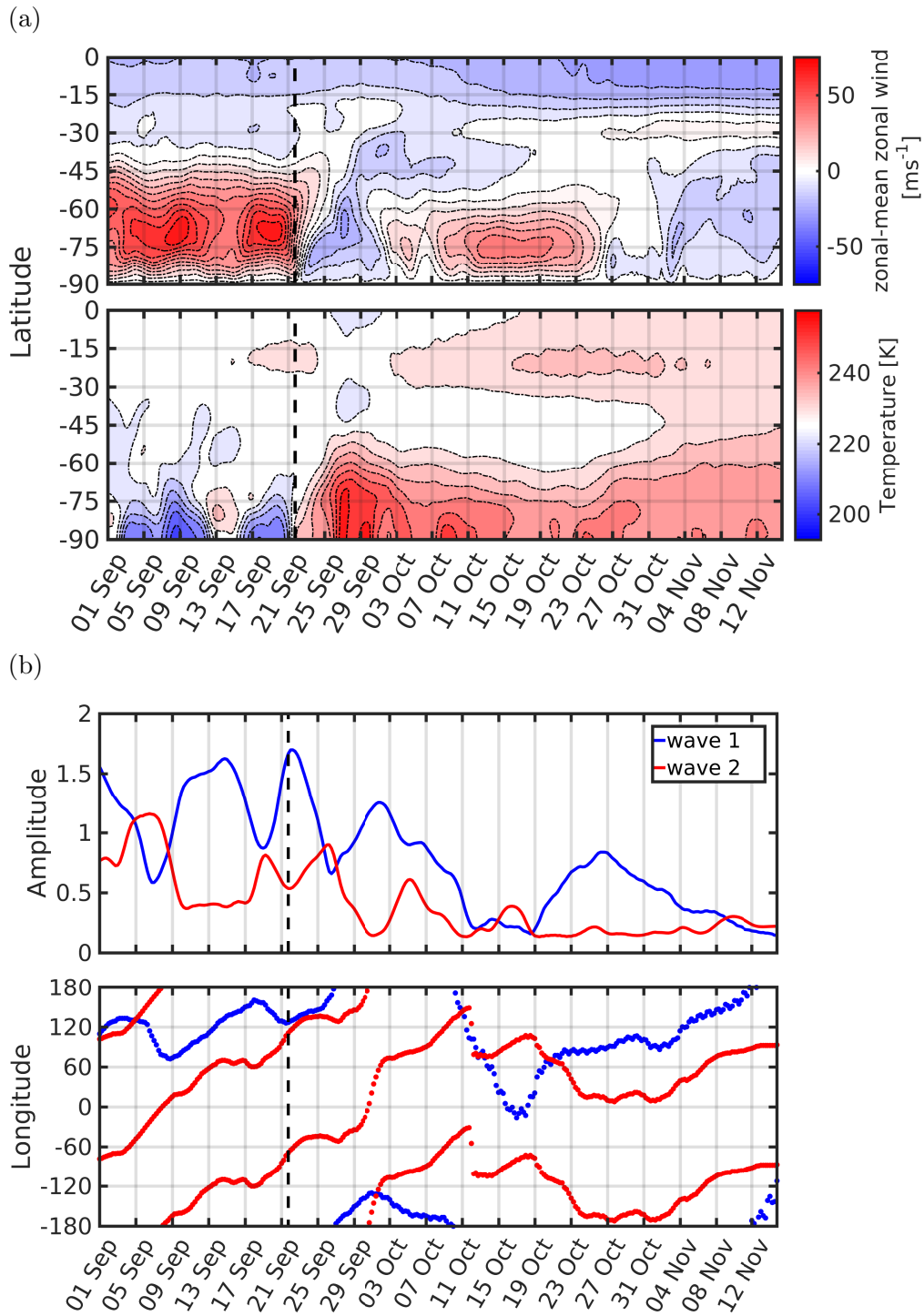


Figure 2: **Eulerian** diagnostics at 10 hPa: (a) Time - latitude diagrams at 10 hPa of the zonal mean velocity (m s^{-1}) and temperature (K). (b) Time series at 60° S for wave 1 (blue) and wave 2 (red), amplitudes [km] (upper panel) and location of the ridges (lower panel). September 22 is marked with a vertical black dashed line.

evolves forwards and backwards in time for a time interval τ .

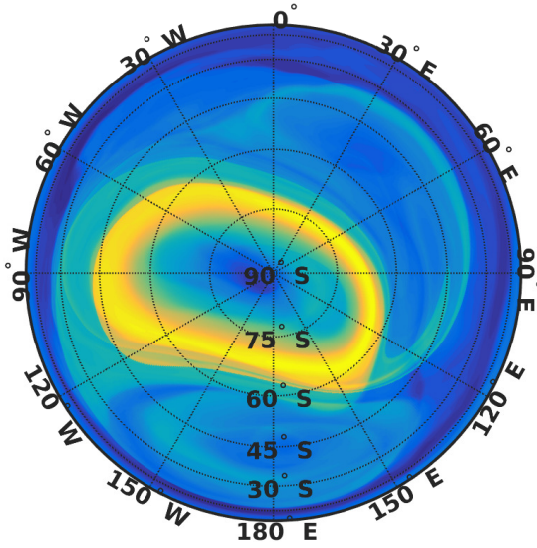
Despite its simple physical interpretation, the function M is a powerful tool for finding the dynamical objects of interest for our study [19, 20, 21, 22]. Stratospheric flows on the timescale of sudden warmings (~ 10 days) are, to a first approximation, adiabatic and frictionless, which justifies their study in 2D isentropic (i.e. constant potential temperature) surfaces. Systematic numerical experimentation by [20, 23] have demonstrated that singular features of M in 2D flows are aligned with invariant curves of the system (invariant manifolds). Moreover, the crossing points of such invariant curves represent trajectories of system. On the basis of such findings, [20, 23] conjectured that for sufficiently large values of τ , large magnitudes of ∇M highlight the stable and unstable manifolds and, at their crossings, hyperbolic points. Some analytical results in this regard are discussed in [21]. Accordingly, cross-hatched patterns of M in a color-coded plot can be associated with the intersection of unstable and stable manifolds and associated hyperbolic points, whose instantaneous locations for time-dependent flows are points on hyperbolic trajectories. [22] discuss particular examples in which contour plots of a Lagrangian descriptor may not clearly capture the presence of singularities, but the velocity fields in these examples are not representative of the ones found in the geophysical context considered in the present paper. In view of these demonstrated properties, M has already been successfully applied in studies on dynamical and transport processes in the stratosphere ([24, 17, 25, 26, 27, 12]).

Figure 3 shows stereographic projections of the function M evaluated using $\tau = 5$ days on the 850 K isentropic surface for the same days as Figure 1. In this case, the trajectories are calculated using the horizontal wind velocity components (interpolated to isentropic surfaces) which are available from the ERA-Interim four times daily (00:00, 06:00, 12:00, 18:00 UTC) with a horizontal resolution of $0.75^\circ \times 0.75^\circ$ in longitude and latitude. Details on the calculation of trajectories from a given velocity field can be found in Garcia-Garrido et al, (2017). The pattern similarity between PV and M plots is strong. The PV plots emphasize the high values associated with the SPV and the detailed structure of the surrounding flow in what is known as the “surf zone” where Rossby waves break (see [28]). High (low) values of M correspond to long (short) trajectories during the time interval $(t_0 - \tau, t_0 + \tau)$, as is the case at locations along (away from) the jets. The time averaging in M can blur some features with small spatial and time scales, but the ability to provide the locations of the hyperbolic trajectories has many advantages for stratospheric studies. Thus, the PV and M diagnostics complement each other well for Lagrangian analyses of the stratospheric circulation.

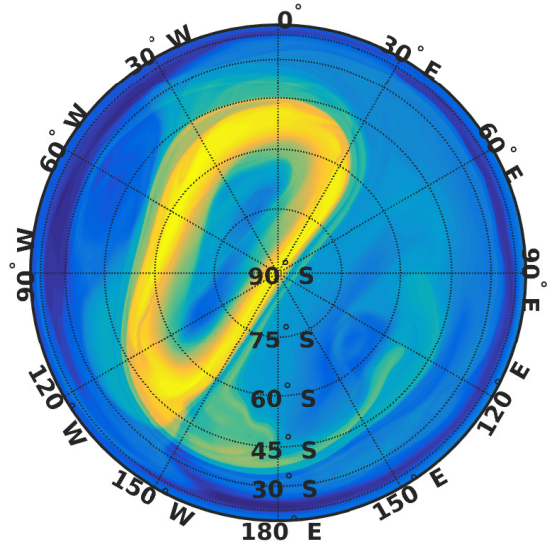
3.2 The kinematic model (KM)

The flow in the real atmosphere is very complex. To gain insight into the fundamental mechanisms at work for transport processes it is useful to have a simple model that focuses on the behavior of the longest planetary waves and that allows for a series of sensitivity experiments. Therefore, we have devised a simple KM in which the amplitude and phase

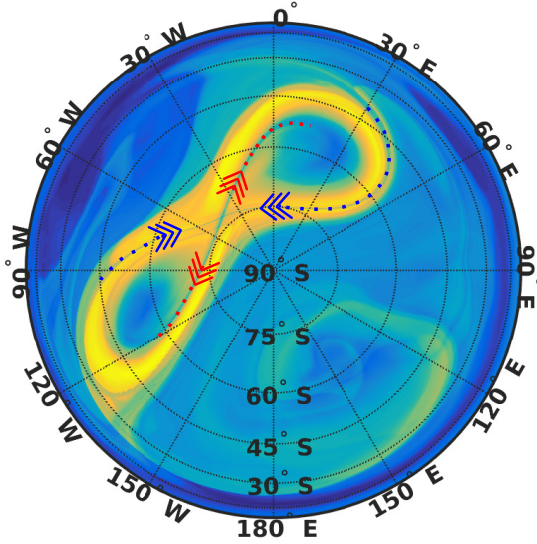
(a) 9 September 2002



(b) 22 September 2002



(c) 24 September 2002



(d) 15 October 2002

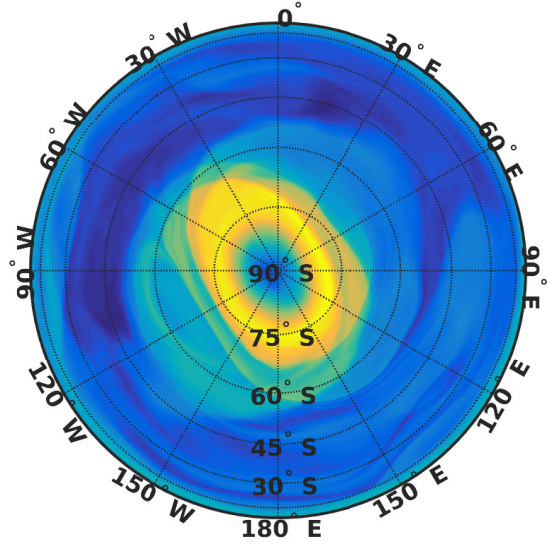


Figure 3: The normalized function M ($\tau = 5$) at 850K for the same days as in Figure 1. In all figures of M in this paper, the bright yellow color represents high values (i.e., long parcel trajectories in $(t_0 - \tau, t_0 + \tau)$) and the dark blue color represents small values (i.e., short parcel trajectories in $(t_0 - \tau, t_0 + \tau)$). The blue and red arrows in (c) indicate the stable and unstable manifolds respectively.

speed of the waves can be specified analytically or according to observations. [12] demonstrate that one such model with a suitable choice of parameters is able to produce strikingly similar transport features to those found in the reanalysis data, including filamentation and vortex breakdown. The KM in [12] consists of a vortex centered at the origin of a cylindrical coordinate system (r, λ) plus two perturbations representing the Fourier components with wavenumbers 1 and 2 along “latitude circles” (lines of constant r); these perturbations can rotate in time around the origin. The vortex and perturbations dependence on r are chosen to mimic the structures of the zonal mean jet and longest planetary waves in September 2002. [12] gives details on the KM numerics and calculation of trajectories.

In the present paper we use a slightly modified version of the KM in [12]. Let us consider the cylindrical system of coordinates (r, λ) centered at $(0, 0)$. In our KM, the velocity field corresponds to an axisymmetric vortex centered at $(x_0, y_0) = (r_0 \cos(\lambda_0), r_0 \sin(\lambda_0))$, plus a perturbation with wavenumber 2 only around $(0, 0)$. Thus, in our case, the effect of wave 1 (and other harmonics) appears in the displacement of the vortex from the origin $(0, 0)$. This modification allows for non-zero velocities across the origin $(0, 0)$, which are not defined in the version by [12], but were present during the vortex splitting under consideration. The equation for the streamfunction in our KM is given by,

$$\Psi(r', r, \lambda, t) = \varepsilon_0(t)F_0(r') + \varepsilon_2(t)\Psi_2(r, \lambda), \quad (3)$$

where r' is the distance to (x_0, y_0) . The first term in the right-hand-side of (3) represents an axisymmetric vortex centered at (x_0, y_0) , and the second term represents a standing wave with zonal wavenumber 2 around $(0, 0)$. The amplitudes ε_0 and ε_2 are given by,

$$\varepsilon_0(t) = \eta_0(1 + \sin(\mu_0 t + \pi)), \quad (4)$$

$$\varepsilon_2(t) = \eta_2(1 + \sin(\mu_2 t)) \quad (5)$$

Note that the intensity of the vortex and amplitude of the wavenumber 2 perturbation can vary in time such that one increases when the other decrease and vice versa in a very primitive representation of wave-mean flow interactions.

The specific structural forms of F_0 and Ψ_2 in our KM are given by,

$$F_0(r') = e^{-r'}(a r' + a - r'(r' + 2) - 2), \quad (6)$$

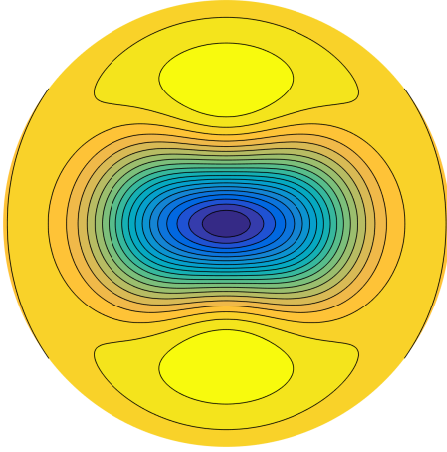
$$\Psi_2(r, \lambda) = r^2 e^{-r^2} \sin(2\lambda + \pi/2). \quad (7)$$

These specific forms are inspired by the corresponding structures in the observational data for September 2002. Figure 4(a) shows that the streamfunction in the KM for $a = 2, \mu_0 = 0, \mu_2 = 2\pi/10, \eta_0 = 2.5, \eta_2 = -1$ and $t = 0$ closely resembles the observed geopotential field at 10 hPa on 9 September 2002 (Figure 4(b)).

The KM with the appropriate parameters can also capture the spectral distribution of observed velocities. [25] associate the jet with values of M that are above a certain

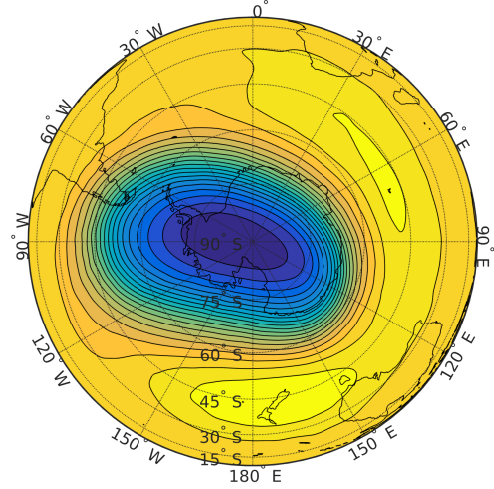
Kinematic Model

(a)

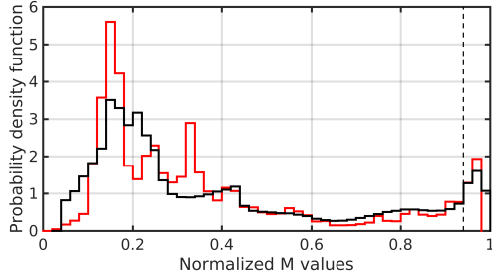


Reanalysis Data

(b)



(c)



(d)

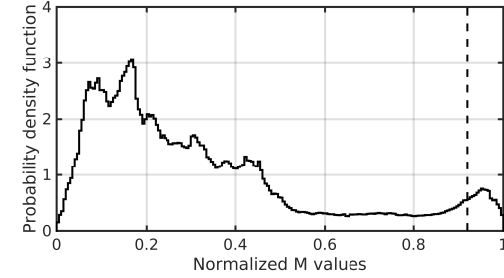


Figure 4: (a) $-\Psi$ given by equation (3) with parameters $a = 2$, $\mu_0 = 0$, $\mu_2 = 2\pi/10$, $\eta_0 = 2.5$, $\eta_2 = -1$, and axisymmetric vortex centered at the origin at $t = 0$. There are 20 contour lines between 0 (blue) and 1.4214 (yellow) uniformly distributed. (b) Orthographic projection of the geopotential height field for the 10 hPa pressure level on 9 September 2002 at 00:00:00 UTC. There are 20 contour lines between 27.5km (blue) and 31.3km (yellow) uniformly distributed. (c) Probability density function estimate for the normalized function M computed with $\tau = 5$ (black line) and $\tau = 15$ (red line) over a period of ten days. The area of each bar is the relative number of observations in the bin; hence the area under the curve is 1. The dashed line corresponds to normalized M equal to 0.94. (d) Probability density function estimate of the normalized function M ($\tau = 5$) at 850K for a ten-day period centered on 9 September 2002. The dashed vertical line corresponds to 0.92.

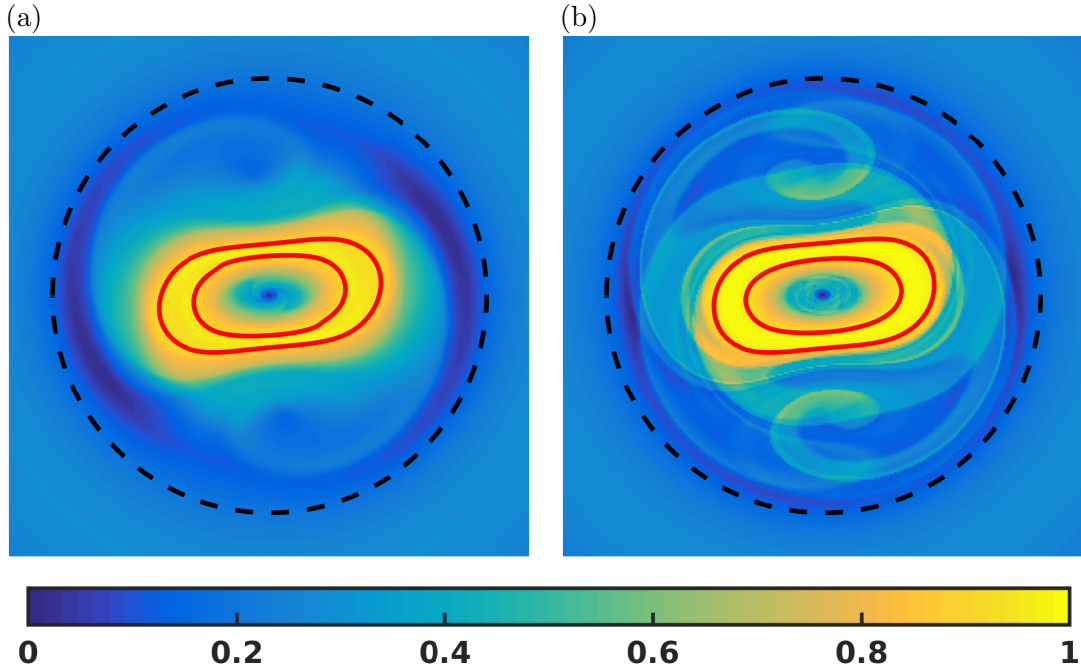


Figure 5: The normalized function M obtained at $t = 0$ computed with $\tau = 5$ (a) and $\tau = 15$ (b) from the KM (3) with parameters $a = 2$, $\mu_0 = 0$, $\mu_2 = 2\pi/10$, $\eta_0 = 2.5$, $\eta_2 = -1$ and $(x_0, y_0) = (0, 0)$. The red lines are the contours of normalized M equal to 0.94. We note the increasing richness in detail with increasing τ .

threshold found by inspection of the probability distribution function (PDF) of M . The PDF resembles a Gaussian distribution with a fat tail. We plot in Figure 4(c) the PDF of M for the same parameters used obtain Figure 4a) for two different values of τ . Figure 4(d) show PDFs of M ($\tau = 5$) at 850K for a ten-day period centered on 9 September 2002. Again, the similarity between KM fields and observations is apparent.

4 Introduction of a definition for the vortex boundary based on M

In terms of the PV field, the SPV edge on an isentropic surface has been indicated simply by an isoline determined by inspection [29, 30, 27], using the total ozone field [31], or by the latitude across which the meridional gradient PV field is maximum for a particular longitude ([28, 32, 17]). A vortex border region has also been defined as a domain bounded by PV isolines (e.g., [33, 34, 35]).

The computation of PV maxima at particular longitudes can produce ambiguous results, especially when the vortex splits or is no longer around the pole as meridians may

intersect more than one vortex edge. In order to bypass this difficulty, [36] choose the location of the polar vortex boundary using a methodology in which PV is expressed as a function of a single variable: the equivalent latitude. For a value of PV, its equivalent latitude (ePV) is defined as that of the border of a polar cap with the same area as the one enclosed by the PV isoline on the isentropic surface. The one-dimensional function ePV may have several local maxima. The special PV isoline that defines the vortex edge is defined as the one where the derivative of ePV is maximum and is near the location of the maximum wind speed calculated along the PV isolines. [25] mentions that the equivalent latitude of the vortex edge can be defined as that where the “impermeability function” is maximum, in which this function is defined as the product of the derivative of ePV times the velocity also expressed as a function of equivalent latitude. Definitions that use the concept of equivalent latitude generally result in closed isolines of PV around local maxima of this field, which can be more than one as it occurs when the vortex splits.

There are also definitions that employ Lagrangian concepts. [37] define the vortex edge as the PV contour with the minimum flux of parcels across it. [38] estimates the structure of the polar vortex with a technique that finds regions with minimal external transport based on transfer operators. [39] define the vortex edge on isentropic surfaces on the basis of Lagrangian Coherent Structures (LCSs). They show that a curve defined as the outermost elliptic LCS around the polar vortex region forms an optimal, non-filamenting transport barrier dividing the vortex core from the surf zone.

We are interested in revisiting the definition of the SPV boundary in order to help with the selection of parcel trajectories that will be used in Part II to visualize the 3D evolution of the event. In our scenario, the boundary region of a vortex would be such that, (i) it divides the core from its surroundings, and (ii) it is free of hyperbolic trajectories and hence does not produce filaments during a certain time interval. A region with these properties, if it exists, would emulate a transport barrier between the vortex core and the “surf zone” during a time interval to be specified.

Let us examine the problem of finding a region with such properties in the context of the KM given by a circumpolar jet plus a standing wave 2 both with a time varying amplitude and the following set of parameters: $a = 2, \mu_0 = 0, \mu_2 = 2\pi/10, \eta_0 = 2.5, \eta_2 = -1$. For a given sufficiently large τ , the region with values of M above a sufficiently high threshold would satisfy requirement (i) because trajectories will tend not to cross locations characterized by parcels that travel at the highest speeds throughout the interval $(t - \tau, t + \tau)$, such as those in the jet itself. Typically jets are characterised by the trajectory geometry and also in terms of particle speed since those in the jet travel faster than those outside the jet. A reasonable choice for the threshold is the lower limit of the fat tail in the PDF of M , as marked in Figure 4(c) and which corresponds to the upper 94 per cent of the values (normalized $M=0.94$). The two isolines corresponding to this threshold are shown in red in Figure 5. (Note that despite the increased richness in M details with a higher τ , the threshold value is practically the same.) To address requirement (ii) we recall that [20, 23] conjectured that for sufficiently large values of τ , cross-hatched patterns in a color-coded

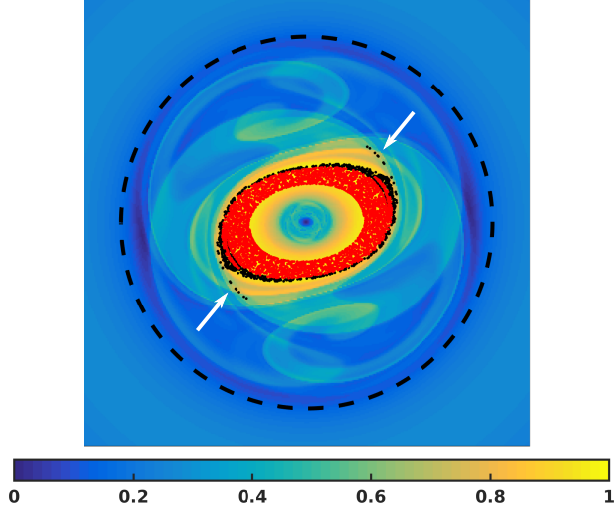


Figure 6: The function M ($\tau = 15$) obtained at $t = 29$ from the KM (6)-(7) with parameters $a = 2$, $\mu_0 = 0$, $\mu_2 = 2\pi/10$, $\eta_0 = 2.5$, $\eta_2 = -1$ and $(x_0, y_0) = (0, 0)$. The red points are the position of the particles that at time $t = 0$ are between the two red lines of Figure 5, i.e. they have values of normalized M larger than 0.94. The black points are the position of the particles that have at time $t = 0$ values of normalized M between 0.89 and 0.94. The white arrows highlight the hyperbolic points.

plot of M can be associated with the intersection of unstable and stable manifolds of associated hyperbolic trajectories. It is reasonable to assume that no such structures form in the narrow confines of the two red curves in Figure 5, at least for the values of τ used in the KM integration (5 and 15). Hence, we posit that the region between the red curves represents a barrier without (or with minimum) filamentation in the interval $(-\tau, \tau)$.

To verify the plausibility of identifying the region delimited by the isolines determined using the PDF of M with a kinematic vortex boundary, we examine the parcel trajectories. First, we select at $t = 0$ parcels within the two red curves in Figure 5 (i.e., normalized M larger than 0.94), and label them with red dots. Second, we take parcels just along and outside of the outer red curve in Figure 5 (i.e., $0.89 \leq \text{normalized } M \leq 0.94$), and label them with black dots. The position of the selected parcels at $t = 29$ are indicated in Figure 6. We can see that red dots have remained within the region we are referring to as the kinematic vortex boundary. Although most black dots have remained also close to the outer red curve, however, we can also see two filaments of black dots associated with the hyperbolic trajectories highlighted by the arrows. We conclude that our procedure can provide the approximate location of the poleward boundary of the “surf zone” as well as the equatorward boundary of the vortex interior.

A more formal approach to describing the boundary of the jet that forms the SPV is discussed by [40]. Their approach is based on the presence of dynamical barriers formed by fluid parcels evolving in closed trajectories, i.e. periodic trajectories, that trap regions of

fluid in their interior. Mathematically these objects are denoted as tori. In 2D incompressible stationary flows, these closed trajectories are related to level sets of a streamfunction that at all times would resemble that depicted in Figure 4a). In these cases, the periodic trajectories are characterized by a single frequency and for this reason are called 1-tori. A single closed contour of the stationary streamfunction is an invariant set (see the annex A for this definition) and therefore it is a barrier to transport. If the fluid is subjected to certain classes of time-dependent perturbations, some nonchaotic trajectories survive in the perturbed system. The conditions for this to occur are given by the Kolmogorov-Arnold-Moser (KAM) theorem [40, 41]. These trajectories, which are characterized by a higher number of frequencies and are called n-tori, still have the ability to trap fluid in their interior, and are therefore barriers to transport. Unfortunately in fluid flows subjected to time dependent perturbations, as the ones we are considering in the present study, periodic solutions related to tori cannot be obtained from the contourlines of the streamfunction. The recent paper by [22] provides a way to compute tori by using the function M . This methodology is firmly rooted in results of the Birkhoff ergodic theorem, which is applicable in this case since the flow represented by our KM has a Hamiltonian structure and is defined on a bounded domain ([12]). Under these conditions Birkhoff ergodic theorem states that the function M divided by 2τ , i.e. the average of $|\mathbf{v}(t, x, y)|$ along the trajectory, converges in the limit $\tau \rightarrow \infty$. The contours of these limit values are invariant sets. We next discuss how a numerical implementation of this result in the KM provides an approach to a 2-torus, which provides a boundary region for the vortex.

Let us compute the average of $M/(2\tau)$ as a function of τ for the points $(x_0, 0)$ along the black line in Figure 7(a). Figure 7(b) shows that this average approximately converges for $\tau \sim 300$ if x_0 belongs to the interval $[0.8, 1.29]$. In our scenario, we consider that these results provide a sufficient, albeit not a rigorous, evidence of convergence in the limit $\tau \rightarrow \infty$.

We contrast the different behaviours obtained for points inside and outside this interval by showing in different coloured lines in Figure 7(c) the variation of $M/(2\tau)$ with τ for initial conditions $(0, 1.36)$, $(0, 1.29)$, $(0, 0.8)$ and $(0, 0.51)$. Starting at $(0, 1.36)$ the purple line in Figure 7(c) (see also purple point in Figure 7(a)) reveals that convergence is not reached for $\tau \sim 300$, and hence contourlines do not correspond to invariant sets. Similarly, convergence is not obtained in the interior part of the vortex starting at $(0, 0.51)$, according to the wine line in Figure 7(c) (see also the wine point in Figure 7(a)). Starting at $(0, 1.29)$ the blue line reveals that convergence is approached for $\tau \sim 300$. We can see in Figure 7(a) that the blue contour marks an approximate outer edge for the vortex. Similarly, the green line obtained starting at $(0, 0.8)$, shows the convergence for $\tau \sim 300$. Figure 7(a) also shows that the cyan contour marks an approximate edge for the vortex interior. Contourlines taken on $M/(2\tau)$, when this has converged in τ , do correspond to invariant sets. Movie S1 in the supplementary material shows the evolution of particle trajectories placed on and outside a 2-torus. The coincidence between the outer and innermost invariant sets with the contours shown in Figure 5 (b) corresponding to the values of M given by the

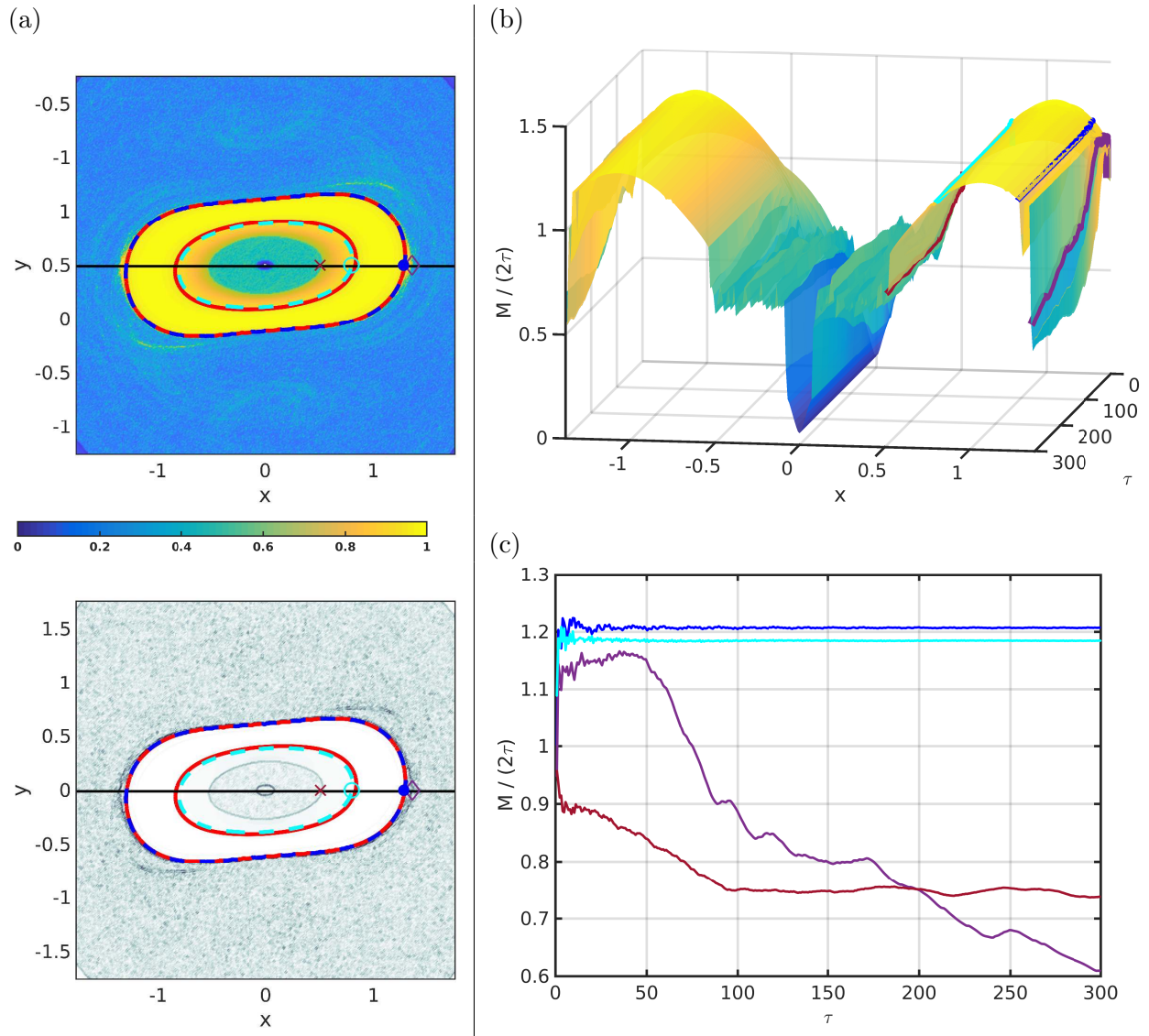


Figure 7: (a) The function M (top) and ∇M (bottom) obtained at $t = 0$ with $\tau = 300$. The dashed blue and green contourlines mark the approximate outer and inner boundaries for the vortex, respectively as defined by the contours of normalized M equal to 0.94 (red lines). The purple diamond, blue point, cyan circle and wine cross in the panels of the left column correspond to points just outside, on the outer boundary, on the inner boundary, and just inside the vortex boundary. (b) Values of M divided by 2τ in the range $\tau \in (0, 300]$ for trajectories obtained from initial conditions along the solid black line of (a). The colours identify the location of the initial conditions in reference to the upper panel of (a). (c) Time evolution of M divided by 2τ for the trajectories from initial conditions corresponding the blue, cyan, purple and wine points in (a). Note that M divided by 2τ does not converges as τ increases for trajectories with initial conditions outside the vortex boundary.

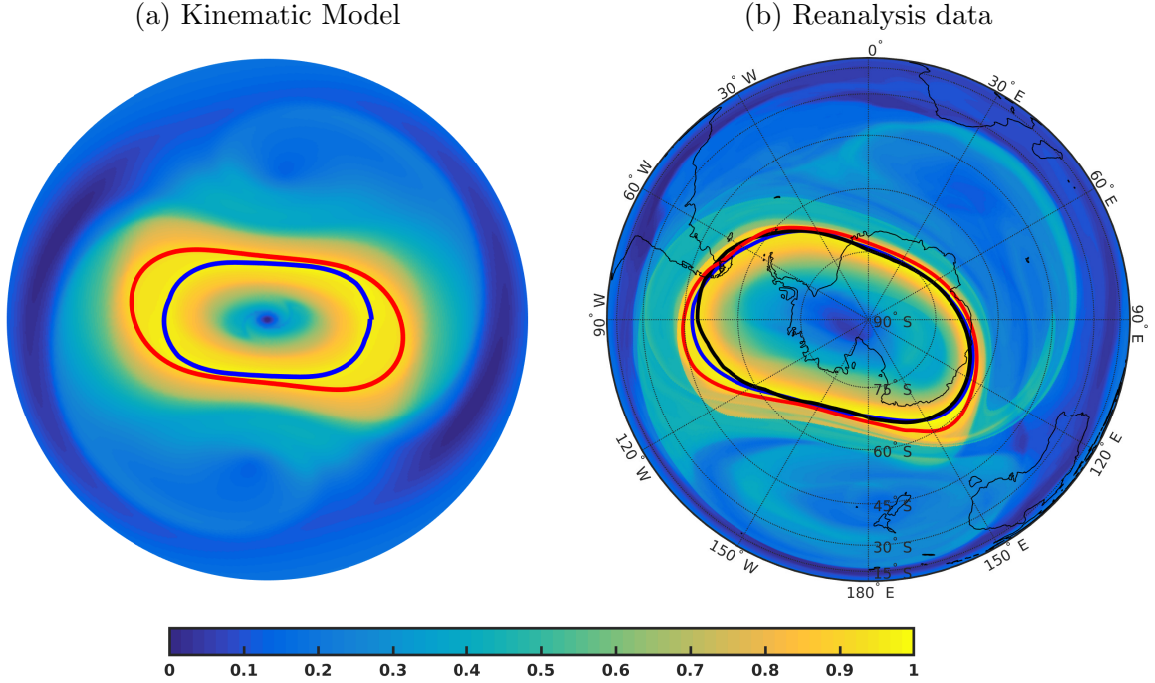


Figure 8: On a background depicting the function M ($\tau = 5$) at $t = 5$ (a) and 9 September 2002 at 850K (b), the colored lines correspond to different ways to identify the vortex edge. Blue. Maximum of M (eq. 2) for each longitude. Red: Outer contour of normalized M equal to 0.92. Black (in (b) only): Maximum of the PV gradient (∇PV) for each longitude. All curves were smoothed by application of a running average of one degree of latitude (20 points).

PDF, confirms that the heuristic approach discussed above can be justified on the basis of concepts from ergodic theory. The rigorous mathematical justification, however, can be obtained only in periodic or quasi periodic cases [42, 43]. This is because the Birkhoff ergodic theorem has not been proven for aperiodically time dependent velocity fields.

Nevertheless, there is computational evidence that this methodology is valid more generally. The supplementary material includes a plot similar to Figure 5(a), except for the addition of a small (5%) random perturbation to the amplitude of wave 2 in the KM. The figure shows similarities between the vortex edge defined by the PDF in the periodic and random perturbation cases. Caution must be exercised in assigning a general character to this result because [21] discuss an example in which for sufficiently long τ , tori-like structures are broken in the case of aperiodic forcing, even for amplitudes one-order of magnitude smaller than those used in the periodic forcing.

Thus, we have three candidates for the determination of the vortex edge. These are listed below, to be applied on isentropic surfaces as well as on surfaces of constant height.

- (i) Maximum of ∇PV for each longitude,

- (ii) Maximum of the function M (eq. 2) for each longitude,
- (iii) Outer most contour of M for a boundary obtained by inspection of the PDF (our proposal).

The colored lines in Figure 8 show the curves obtained with the different definitions of the vortex edge for 9 September 2002 at 850K. On this day and isentropic surface, the SPV was circumpolar albeit elongated and a broad filament had formed in the 130° E - 150° E sector. According to Figure 8(b), there are particles outside the region bounded by the lines (i)-(iii) that after 5 days remain inside the vortex edge. In Part II we will be particularly interested in the behaviour of these particles, as they will tend to be “peeled off” the vortex along filaments. This can be seen in the video S2 provided in the supplementary material.

5 Criterion for vortex splitting

In this section we examine the vortex splitting. The function M at 850K computed from reanalysis data for 24 September 2002, just at the time of the observed split before the vortex breakup, is shown in Figure 3(c). We can obtain a highly similar structure in the KM by properly selecting the model parameters using a strong wave 2 increasing in amplitude and a substantial contribution from a vortex with a center displaced from the pole.

The left panel in Figure 9(a) shows the function M from the KM at $t = 3$ with $a = 2$, $\mu_0 = 2\pi/50$, $\mu_2 = 2\pi/30$, $\eta_0 = 2.5$, $\eta_2 = -1$ and $(r_0, \lambda_0) = (0.75, \pi/2)$. At $t = 3$, the KM with this set of parameters models a circular vortex displaced from the pole whose intensity is decreasing with time, and a wave 2 centered at the pole whose amplitude is increasing with time. Also note that the cyclonic vortex lies above an anticyclonic lobe of wave 2. A hyperbolic trajectory can be clearly seen at a location close to the pole in the plot of ∇M displayed in the right panel of the figure. The global structure of the manifolds depends not only on local aspects in the neighbourhood of a hyperbolic trajectory, but also on large-scale aspects of the perturbation. At a later time, $t = 9$, this vortex splits such as shown in Figure 9(b). In this case the perturbation dominates and the splitting occurs.

Not all evolutions of a pinched SPV result in splitting. At $t = 72$, the KM with the same parameters as before models a circular vortex displaced from the pole whose intensity is increasing with time and a wave 2 centered at the pole whose amplitude is decreasing with time. In this case, the pinching structure in Figure 9(c) evolves into one vortex as shown in Figure 9(d).

An examination of the structure of the evolving manifolds intersecting at the hyperbolic trajectory can provide a criterion on whether the split will occur or not. Figure 10 is a schematic of the three possible situations for the manifold structures: (a) the unstable manifold (in red) is in the inside part that delimites the stable manifold (in blue) and no intersection points are detected in the period $(t_0 - \tau, t_0 + \tau)$, (b) the two manifolds are

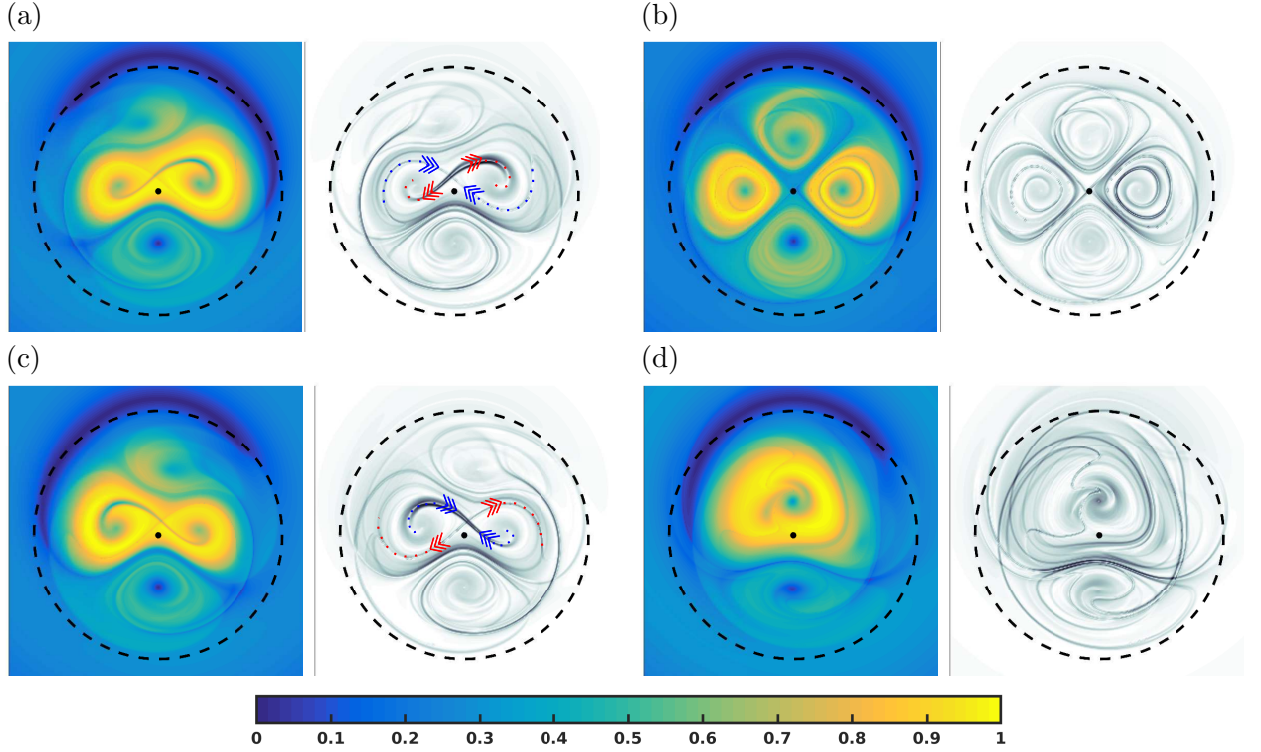


Figure 9: The function M ($\tau = 15$) and ∇M obtained from the KM (6)-(7) at earlier time (left two columns) and later time (right two columns) with parameters $a = 2$, $\mu_0 = 2\pi/50$, $\mu_2 = 2\pi/30$, $\eta_0 = 2.5$, $\eta_2 = -1$ and $(x_0, y_0) = (0, 0.75)$. The pole is marked with a black dot and the equator with a dashed black line. A pinched vortex in (a) and (c) splits into two vortices in (b), or merges into one in (d). The blue and red arrows in panels (a) and (c) over ∇M show the position of the stable and unstable manifolds, respectively in each case. This configuration agrees with the sketch of the structures shown in figure 10, where the particles are organized into two vortices or in a single vortex.

almost symmetric with respect to the observed intersection point opposite to the hyperbolic trajectory of reference, and (c) the stable manifold is in the inside part that delimits the stable manifold and no intersection points are detected in the period $(t_0 - \tau, t_0 + \tau)$. An analysis of particle trajectories in these three instances reveals that in case (a) the structure causes the particles to organize in two vortices, while in cases (b) and (c), after pinching the particles organize in a single vortex. In the KM with the parameters selected, configuration (a) corresponds to $t = 3$, (b) corresponds to a vortex centered at the pole, and (c) to $t = 72$. We will show in Part II that these different structures formed at different levels in the stratosphere in a way consistent with the presence or absence of the vortex splitting in September 2002.

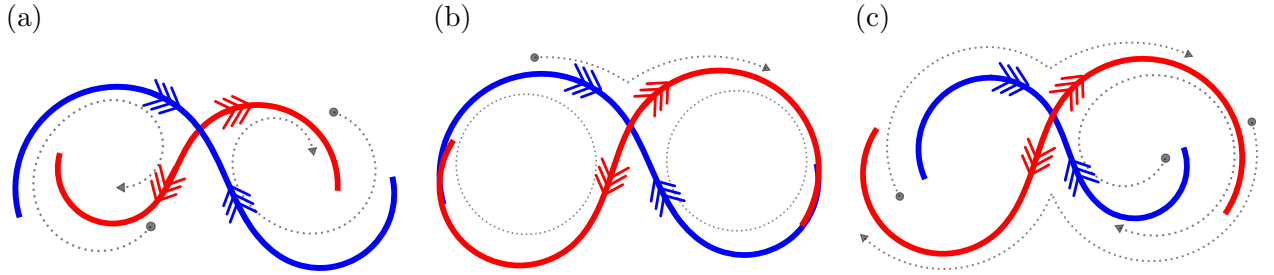


Figure 10: Sketch showing configurations of stable (blue line) and unstable (red line) manifolds according to which one can expect at later times either vortex splitting (a) or no splitting (b) and (c). The grey dashed lines shown schematically the trajectory of particles in the vicinity of the manifolds.

6 Summary and Conclusions

Our goal in the present two-part paper is to provide a Lagrangian perspective of the final southern warming in spring of 2002, during which the stratospheric polar vortex (SPV) experienced a unique splitting. In this Part I, we presented our methodology and concentrate on the fundamental processes for filamentation and ultimately for vortex splitting.

We have worked in the idealized context of a Kinematic Model (KM). The KM aims at emulating the behavior of the longest planetary waves on an isentropic surface as obtained from the reanalysis data, and allows for detailed parametric analysis. Previous studies had demonstrated that one such a model can be defined and applied to examine the mechanisms responsible for complex fluid parcel evolution during the polar vortex filamentation and breakdown. One of our objectives with the KM was to explore a kinematic definition for the SPV boundary that could be justified, at least in some cases, with arguments that go beyond heuristic considerations based on the potential vorticity field as is generally done. The second objective was to gain insight into the role of Lagrangian structures in the SPV splitting.

It was argued that a kinematically meaningful definition of the SPV boundary is the region bounded by the contours of the Lagrangian descriptor known as the function M corresponding to threshold values determined by inspection of probability distribution functions (PDFs) of M . In the context of the KM, this definition of vortex boundary was linked to rigorous results that identify a 2-torus with contours on which the values of $M/(2\tau)$ converge in τ . The outer boundary of this region provides the approximate location of the poleward boundary of the surf zone. We provided examples of how this boundary relates to the formation of filaments in the surf zone. We will use this definition in Part II for the selection of particles whose trajectories will illuminate the SPV behavior in September 2002 at several levels.

Finally, we used the KM to explore different behaviours of the SPV. In particular, we examined two cases in which a pinched vortex evolved into two very different structures.

In one of them the vortex split completely, while in the other case the vortex returned to a less disturbed configuration. An examination of the function M for these cases suggested a criterion to anticipate the vortex behavior. We shall apply this criterion in Part II to justify why the SPV split at some levels in September 2002, while it remained as one in other levels.

A Annex

There exist different dynamical objects that support the qualitative description of particle time evolution. This qualitative description is based on Poincaré’s ideas, and consist of determining geometrical structures that define regions where particle trajectories have qualitatively different behaviours. The boundaries between these regions are dynamical barriers. These geometrical structures provide a template for a specific velocity field and emphasize the essential transport features associated with it.

Hyperbolic trajectories are one type of recognisable dynamical features in flows. These are special trajectories, in the neighbourhood of which air masses are elongated along the unstable direction and compressed along the stable direction. An important feature here is that two parcels placed at nearby locations close to a hyperbolic trajectory may evolve in time quite differently, separating at exponential rates.

Trajectories of particles initially placed in the neighbourhood of a hyperbolic trajectory become aligned as time evolves forward with a curve called the *unstable manifold*; similarly, trajectories of particles in the neighbourhood of a hyperbolic trajectory as time evolves backwards become aligned with a curve called the *stable manifold*. Figure 11(a) illustrate this forwards and backwards alignment of the green blobs with the orange and cyan blobs. For time dependent flows, hyperbolic trajectories do not correspond to hyperbolic instantaneous stagnation points of the velocity field. Their positions can be rather different, thus being the behavior of particles in a time interval quite counter-intuitive from what is observed for a velocity field that is frozen in time.

Stable and unstable manifolds are aligned with singular features of M . Figure 11(b) shows two lines crossing in the middle of the yellowish region. These lines are aligned with the stable and unstable manifolds appearing in panel (a) and correspond, respectively, to the stable and unstable manifolds of the hyperbolic trajectory at the crossing point.

Unstable and stable manifolds are *invariant curves*. This means that as time evolves either forwards or backwards, respectively, particles stay on those curves. Particles do not cross these curves, therefore they are material curves, and are barriers to transport. Stable and unstable manifolds act as repelling and attracting material lines, respectively [44].

Apart from hyperbolic trajectories and their stable and unstable manifolds, other types of dynamical flow structures exist, in which particles tend to stay together, coherently, without dispersing, such as vortices that keep fluid parcels inside them, or jets. Invariant tori are the dynamical objects related to that behaviour. These objects are invariant in

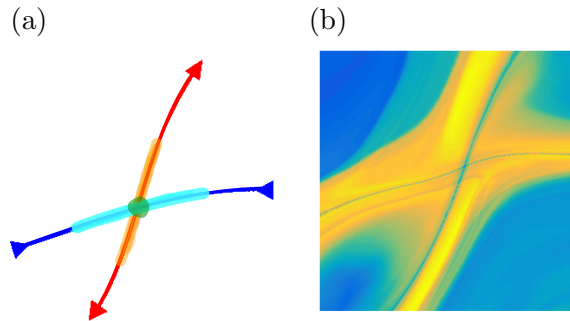


Figure 11: (a) Sketch of a hyperbolic trajectory and its stable (blue line) and unstable (red line) manifolds. Particles in the green blob evolves forwards and backwards in time as the orange and cyan shades respectively. (b) the singular features of M are aligned with the stable and unstable manifolds.

the sense defined above, i.e. particles evolve in time staying on them. Further details on tori are given in Section 4.

Background for this Annex can be found in [45, 46, 47, 48].

Acknowledgements

J. Curbelo and A. M. Mancho are supported by MINECO grant MTM2014-56392-R. A. M. Mancho is supported by ONR. grant No. N00014-17-1-3003. C. R. Mechoso was supported by the U.S. NSF grant AGS-1245069. The research of S. Wiggins is supported by ONR grant No. N00014-01-1-0769. This paper has also received funding from the European Union’s Horizon 2020 research and innovation programme under the Marie Skłodowska-Curie grant agreement No 777822.

References

- [1] C. R. Mechoso, A. O’Neill, V. D. Pope, and J. D. Farrara. A study of the stratospheric final warming of 1982 in the Southern Hemisphere. *Quart. J. R. Meteor. Soc.*, 114:1365–1384, 1988.
- [2] A. J. Charlton, A. O’Neill, W. A. Lahoz, and P. Berrisford. The splitting of the stratospheric polar vortex in the southern hemisphere, september 2002: Dynamical evolution. *J. Atmos. Sci.*, 66:590–602, 2005.
- [3] Costas Varotsos. The southern hemisphere ozone hole split in 2002. *Environmental science and pollution research international*, 9(6):375–6, 11 2002.

- [4] Costas Varotsos. What is the lesson from the unprecedented event over antarctica in 2002. *Environmental science and pollution research international*, 10(2):80–1, 03 2003.
- [5] Costas Varotsos. The extraordinary events of the major, sudden stratospheric warming, the diminutive antarctic ozone hole, and its split in 2002. *Environmental science and pollution research international*, 11(6):405–11, 11 2004.
- [6] Douglas R. Allen, Richard M. Bevilacqua, Gerald E. Nedoluha, Cora E. Randall, and Gloria L. Manney. Unusual stratospheric transport and mixing during the 2002 antarctic winter. *Geophysical Research Letters*, 30(12):n/a–n/a, 2003. 1599.
- [7] Paul Konopka, Jens-Uwe Grooß, Karl W. Hoppel, Hildegard-Maria Steinhorst, and Rolf Müller. Mixing and chemical ozone loss during and after the antarctic polar vortex major warming in september 2002. *Journal of the Atmospheric Sciences*, 62(3):848–859, 2005.
- [8] Yvan J. Orsolini, Cora E. Randall, Gloria L. Manney, and Douglas R. Allen. An observational study of the final breakdown of the southern hemisphere stratospheric vortex in 2002. *Journal of the Atmospheric Sciences*, 62(3):735–747, 2005.
- [9] J. G. Esler and R. K. Scott. Excitation of transient rossby waves on the stratospheric polar vortex and the barotropic sudden warming. *Physical Review E*, 62:3661–3681, 2005.
- [10] G. L. Manney, J. L. Sabutis, D. R. Alley, W. A. Lahoz, A. A. Scaife, C. E. Randall, S. Pawson, B. Naujokat, and R. Swinbank. Simulations of dynamics and transport during the september 2002 antarctic major warming. *J. Atmos. Sci.*, 66(690-707), 2005.
- [11] M. Taguchi. Predictability of major stratospheric sudden warmings of the vortex split type: Case study of the 2002 southern event and the 2009 and 1989 northern events. *J. Atmos. Sci.*, 71:2886–2904, 2014.
- [12] V. J. García-Garrido, J. Curbelo, C. R. Mechoso, A. M. Mancho, and S. Wiggins. A simple kinematic model for the lagrangian description of relevant nonlinear processes in the stratospheric polar vortex. *Nonlinear Processes in Geophysics*, 24(2):265–278, 2017.
- [13] A. Simmons, S. Uppala, D. Dee, and Kobayashi S. ERA-Interim: New ECMWF reanalysis products from 1989 onwards. *ECMWF Newsletter*, 110:25–35, 2007.
- [14] C. R. Mechoso and D. L. Hartmann. An observational study of traveling planetary waves in the southern hemisphere. *Journal of the Atmospheric Sciences*, 39(9):1921–1935, 1982.

- [15] K. P. Bowman. Evolution of the total ozone field during the breakdown of the antarctic circumpolar vortex. *Journal of Geophysical Research: Atmospheres*, 95(D10):16529–16543, 1990.
- [16] G. L. Manney, J. D. Farrara, and C. R. Mechoso. The behavior of wave 2 in the southern hemisphere stratosphere during late winter and early spring. *J. Atmos. Sci.*, 48:976–998, 1991.
- [17] A. de la Cámara, R. Mechoso, A. M. Mancho, E. Serrano, and K. Ide. Isentropic transport within the Antarctic polar night vortex: Rossby wave breaking evidence and Lagrangian structures. *J. Atmos. Sci.*, 70:2982–3001, 2013.
- [18] J. Curbelo, V. J. García-Garrido, C. R. Mechoso, A. M. Mancho, S. Wiggins, and C. Niang. Insights into the three-dimensional lagrangian geometry of the antarctic polar vortex. *Nonlinear Processes in Geophysics*, 24(3):379–392, 2017.
- [19] J. A. J. Madrid and A. M. Mancho. Distinguished trajectories in time dependent vector fields. *Chaos*, 19:013111, 2009.
- [20] C. Mendoza and A. M. Mancho. The hidden geometry of ocean flows. *Phys. Rev. Lett.*, 105(3):038501, 2010.
- [21] A. M. Mancho, S. Wiggins, J. Curbelo, and C. Mendoza. Lagrangian descriptors: A method for revealing phase space structures of general time dependent dynamical systems. *Communications in Nonlinear Science and Numerical Simulations*, 18(12):3530–3557, 2013.
- [22] C. Lopesino, F. Balibrea-Iniesta, V. J. García-Garrido, S. Wiggins, and A. M. Mancho. A theoretical framework for lagrangian descriptors. *International Journal of Bifurcation and Chaos.*, 27(01):1730001, 2017.
- [23] C. Mendoza and A. M. Mancho. The Lagrangian description of aperiodic flows: a case study of the Kuroshio Current. *Nonlin. Proc. Geophys.*, 19(14):449–472, 2012.
- [24] A. de la Cámara, A. M. Mancho, K. Ide, E. Serrano, and C.R. Mechoso. Routes of transport across the Antarctic polar vortex in the southern spring. *J. Atmos. Sci.*, 69(2):753–767, 2012.
- [25] M. L. Smith and A. J. McDonald. A quantitative measure of polar vortex strength using the function m . *J. Gephys.Res. Atmos.*, 119:5966–5985, 2014.
- [26] A. Guha, C. R. Mechoso, C. S. Konor, and R. P. Heikes. Modeling rossby wave breaking in the southern spring stratosphere. *J. Atmos. Sci.*, 73(1):393–406, 2016.

- [27] G. L. Manney and Z. D. Lawrence. The major stratospheric final warming in 2016: Dispersal of vortex air and termination of Arctic chemical ozone loss. *Atmospheric Chemistry and Physics Discussions*, 2016:1–40, 2016.
- [28] M. E. McIntyre and T. N. Palmer. The surf zone in the stratosphere. *Journal of Atmospheric and Terrestrial Physics*, 46(9):825–849, 1984.
- [29] G. L. Manney, R. W. Zurek, M. E. Gelman, A. J. Miller, and R. Nagatani. The anomalous arctic lower stratospheric polar vortex of 1992 - 1993. *Geophysical Research Letters*, 21:2405–2408, 1994.
- [30] D. W. Waugh and W. J. Randel. Climatology of arctic and antarctic polar vortices using elliptical diagnostics. *J. Atmos. Sci.*, 56:1594–1613, 1999.
- [31] K. P. Bowman. Large-scale isentropic mixing properties of the antarctic polar vortex from analyzed winds. *Journal of Geophysical Research: Atmospheres*, 98(D12):23013–23027, 1993.
- [32] M. N. Juckes and M. E. McIntyre. A high-resolution one-layer model of breaking planetary waves in the stratosphere. *Nature*, 328:590–596, 1987.
- [33] T. D. A. Fairlie and A. O’Neill. The stratospheric major warming of winter 1984/85: observations and dynamical inferences. *Quarterly Journal of the Royal Meteorological Society*, 114(481):557–577, 1988.
- [34] B. Tronday, L. Perthuis, S. Strebelle, J. D. Farrara, and C. R. Mechoso. Dispersion properties of the flow in the southern stratosphere during winter and spring. *J. Geophys. Res.*, 100:13901–13917, 1995.
- [35] M. C. Öllers, P. F. J. van Velthoven, H. M. Kelder, and L. P. J. Kamp. A study of the leakage of the antarctic polar vortex in late austral winter and spring using isentropic and 3-d trajectories. *J. Geophys. Res.*, 107(D17):4328, 2002.
- [36] E. R. Nash, P. A. Newman, J. E. Rosenfield, and M. R. Schoeberl. An objective determination of the polar vortex using Ertel’s potential vorticity. *Journal of Geophysical Research: Atmospheres*, 101(D5):9471–9478, 1996.
- [37] S. P. Dahlberg and K. P. Bowman. Climatology of large-scale isentropic mixing in the arctic winter stratosphere from analyzed winds. *Journal of Geophysical Research: Atmospheres*, 99(D10):20585–20599, 1994.
- [38] Naratip Santitissadeekorn, Gary Froyland, and Adam Monahan. Optimally coherent sets in geophysical flows: A transfer-operator approach to delimiting the stratospheric polar vortex. *Phys. Rev. E*, 82:056311, Nov 2010.

- [39] M. Serra, P. Sathe, F. Beron-Vera, and G Haller. Uncovering the edge of the polar vortex. *Journal of the Atmospheric Sciences*, 0(0), 2017.
- [40] I. I. Rypina, M. G. Brown, F. J. Beron-Vera, H. Kocak, M. J. Olascoaga, and I. A. Udovydchenkov. On the lagrangian dynamics of atmospheric zonal jets and the permeability of the stratospheric polar vortex. *J. Atmos. Sci.*, 64:3595–3610, 2007.
- [41] S. Wiggins and A. M. Mancho. Barriers to transport in aperiodically time-dependent two dimensional velocity fields: Nekhoroshev’s theorem and ‘nearly invariant’ tori. *Nonlin. Proc. Geophys.*, 21:165–185, 2014.
- [42] I. Mezic and S. Wiggins. A method for visualization of invariant sets of dynamical systems based on the ergodic partition. *Chaos*, 9(1):213–218, 1999.
- [43] Y. Susuki and I. Mezić. Ergodic partition of phase space in continuous dynamical systems. *Joint 48th IEEE Conference on Decision and Control and 28th Chinese Control Conference*, pages 7497–7502, 2009.
- [44] G. Haller. Lagrangian coherent structures from approximate velocity data. *Phys. Fluids*, 14(1851-1861), 2002.
- [45] J. M. Ottino. *The Kinematics of Mixing: Stretching, Chaos, and Transport*. Cambridge University Press, Cambridge, England, 1989. Reprinted 2004.
- [46] S. Wiggins. The dynamical systems approach to Lagrangian transport in oceanic flows. *Annu. Rev. Fluid Mech.*, 37:295–328, 2005.
- [47] A. M. Mancho, D. Small, and S. Wiggins. A tutorial on dynamical systems concepts applied to Lagrangian transport in oceanic flows defined as finite time data sets: Theoretical and computational issues. *Phys. Rep.*, 237(3-4):55–124, 2006.
- [48] R. Samelson and S. Wiggins. *Lagrangian Transport in Geophysical Jets and Waves: The Dynamical Systems Approach*. Springer-Verlag, New York, 2006.

Jezabel Curbelo

Departamento de Matemáticas
Universidad Autónoma de Madrid
Instituto de Ciencias Matemáticas
Campus de Cantoblanco UAM, 28049 Madrid, Spain.
Email: jezabel.curbelo@uam.es

Carlos R. Mechoso

Department of Atmospheric and Oceanic Sciences,
University of California at Los Angeles

Ana M. Mancho

Instituto de Ciencias Matemáticas, CSIC-UAM-UC3M-UCM.
Campus de Cantoblanco UAM, 28049 Madrid, Spain.

Stephen Wiggins

School of Mathematics, University of Bristol.
Bristol BS8 1TW, UK.